

Niobium-Incorporated CoSe₂ Nanothorns with Electronic Structural Alterations for Efficient Alkaline Oxygen Evolution Reaction at High Current Density

Qimin Peng,^[a] Xiaoling Zhuang,^[a] Longgui Wei,^[a] Luyan Shi,^[a] Tayirjan Taylor Isimjan,^{*,[b]} Ruobing Hou,^[a] and Xiulin Yang^{*,[a]}

Developing cost-effective, highly active, and robust electrocatalysts for oxygen evolution reaction (OER) at high current density is a critical challenge in water electrolysis since the sluggish kinetics of the OER significantly impedes the energy conversion efficiency of overall water splitting. Here, a 1D nanothorn-like Nb–CoSe₂/CC (CC = carbon cloth) structure was developed as an efficient OER catalyst. The optimized Nb–CoSe₂/CC catalyst exhibited remarkable OER performance with the low overpotentials of 220 mV at 10 mA cm⁻² and 297 mV 200 mA cm⁻² and a small Tafel slope (54.1 mV dec⁻¹) in 1.0 M KOH electrolyte. More importantly, the Nb–CoSe₂/CC electrode displayed superior stability after 60 h of continuous operation. In addition, cell voltages of 1.52 and 1.93 V were

required to achieve 10 and 500 mA cm⁻² for the electrolyzer made of Nb–CoSe₂/CC (anode) and the Pt/C (cathode). Density functional theory (DFT) calculations combined with experimental results revealed that incorporating niobium into the CoSe₂ could optimize the adsorption free energy of the reaction intermediates and enhance the conductivity to improve the catalytic activity further. Additionally, the super-hydrophilicity of Nb–CoSe₂/CC resulting from the surface defects increased the surface wettability and facilitated reaction kinetics. These results indicate that Nb–CoSe₂/CC intrinsically enhances OER performance and possesses potential practical water electrolysis applications.

Introduction

The rapidly increasing energy consumption and deteriorating global environmental issues call for the urgency of developing sustainable and carbon-neutral energy storage and conversion technologies.^[1] Hydrogen (H₂), as an ideal chemical energy carrier, has been considered to dominate future energy resources owing to its high energy density and clean pollution-free characteristic. Therefore, electrocatalytic water splitting (2H₂O → O₂ + 2H₂) is advocated as one of the most suitable techniques to produce hydrogen.^[2] Nevertheless, the critical challenge originates from the intrinsically sluggish dynamics of anodic oxygen evolution reaction (OER) involving complex proton-coupled electron transfer, which leads to energy waste and dramatically hinders the realization of high-efficiency water electrolysis. Reducing the activation energy barriers of the OER process decreases the overpotential, which is a significant step for achieving large-scale applications.^[3]

Although Ru/Ir oxides show remarkable activity and stability toward OER, their wide application is severely restricted by exorbitant price and low reserves. As a result, it is urgent to explore inexpensive, Earth-abundant, and non-noble metal OER catalysts with similar activity and durability.^[4]

At present, rapid progress has been achieved in designing transition metal OER catalysts containing selenides, phosphides, oxides, sulfides, carbides,^[5] and so on. Due to the inherent metallic nature, transition metal selenide (TMS) has high conductivity and more active edge sites. The distinct properties show bright prospects in electronics, photodetectors, and semiconductors and have garnered significant attention.^[6] Especially from the electronic configuration perspective, the typical CoSe₂ has a t_{2g}⁶e_g¹ electronic configuration detached from Co 3d electrons, which is close to an ideal electronic e_g filling.^[7] Specifically, it has been reported that an optimal OER catalyst can be obtained when the surface e_g of the transition metal is filled.^[8] However, under highly oxidative conditions such as OER, the monometallic selenide-based catalysts suffer from severe aggregation resulting in insufficient active catalytic sites and poor electrical conductivity.

The above shortcomings can be addressed by introducing a foreign transition metal to tailor the electronic structure of TMSs, which enhance electrical conductivity and tune electronic structures to improve OER electrocatalytic performance significantly.^[9] For instance, the OER of CoP was dramatically enhanced with Cr doping, which effectively adjusts the d-band center and electronic structure.^[10] Furthermore, Nb-doped layered FeNi phosphide with high conductivity and abundant active sites displayed an excellent OER activity.^[11] Special

[a] Q. Peng, X. Zhuang, L. Wei, L. Shi, Prof. R. Hou, Prof. Dr. X. Yang
Guangxi Key Laboratory of Low Carbon Energy Materials, School of Chemistry and Pharmaceutical Sciences
Guangxi Normal University
Guilin 541004 (P. R. China)
E-mail: xlyang@gxnu.edu.cn

[b] Dr. T. T. Isimjan
Saudi Arabia Basic Industries Corporation (SABIC)
King Abdullah University of Science and Technology (KAUST)
Thuwal 23955-6900, Saudi Arabia
E-mail: isimjant@sabic.com

 Supporting information for this article is available on the WWW under <https://doi.org/10.1002/cssc.202200827>

attention has been paid to Nb since it has multi chemical valences ranging from +1 to +5^[12] and exhibits a unique physicochemical nature, high hardness and melting point, and good electrochemical performance.^[13] The Nb improves the catalytic performance from two aspects. On the one hand, it combines with most elements to tune their electronic structures; on the other hand, the Nb atom offers more binding sites to link the active sites, thereby improving the catalytic performance.^[14] Nevertheless, there is no report on Nb doping on Co-based OER catalysts to the best of our knowledge.

We expect an elevated OER activity when CoSe₂ is incorporated with the Nb based on the above observation. Here, we successfully manipulate the CoSe₂ nanothorns for alkaline overall water splitting by adjusting the electronic structure by Nb incorporation. The synthesized Nb–CoSe₂/CC catalyst integrates the unique advantages, comprising the favorable reaction kinetics of the synergistic effects between Co and Nb atoms, electron-rich nanothorn structure, and self-supported robust structure. Incorporating Nb with CoSe₂ showed a significant lower OER overpotential of 220 mV at 10 mAcm⁻² and a small Tafel slope (54.1 mVdec⁻¹) compared to the state-of-the-art OER catalyst (RuO₂) under the same condition. Besides, it revealed excellent durability up to 60 h without apparent attenuation of catalytic activity. Density functional theory (DFT) calculations and the detailed characterizations showed that such outstanding OER activity was correlated with optimized adsorption free energy and enhanced conductivity of reaction intermediates. The results indicate that the Nb incorporation alters the electronic structure of CoSe₂ in

a way that facilitates the adsorption of oxygen-containing intermediates and the O₂ desorption during the OER process. Besides, the increased surface hydrophobicity is beneficial to enhancing the reaction kinetics.

Results and Discussion

Crystal structures and microstructure analysis

As briefly exhibited in Figure 1a, Nb–CoF_{1.3}(OH)_{0.7}/CC (CC = carbon cloth) is firstly obtained by in-situ growth in aqueous solvents. Afterward, the target Nb–CoSe₂/CC was synthesized through a two-step process: hydrothermal selenization and Ar annealing of Nb–CoF_{1.3}(OH)_{0.7}/CC. The prepared Nb–CoSe₂/CC owns a nanothorn structure with open channels and high conductivity, ensuring the rapid release of O₂. The samples' crystal structure was analyzed by X-ray diffraction (XRD). As shown in Figure S2a, the diffraction peaks of the Nb–CoF_{1.3}(OH)_{0.7}/CC are well-matched with CoF_{1.3}(OH)_{0.7}/CC (JCPDS: 18-0405),^[15] and the crystal structure has changed corresponding to Nb–CoSeO₃·2H₂O/CC (Figure S2b) after the hydrothermal selenization. Meanwhile, the XRD patterns of Nb–CoSe₂/CC and CoSe₂/CC are basically consistent with the orthorhombic/cubic CoSe₂ (JCPDS: 10-0408 and 09-0234) (Figure 1b),^[16] where the main characteristic diffraction peaks at 30.8, 34.7, 36.3, and 47.8° are assigned to the orthorhombic (110), (111), (012), and (121) planes, respectively. The peak located at 26° corresponds to amorphous carbon. Besides, other

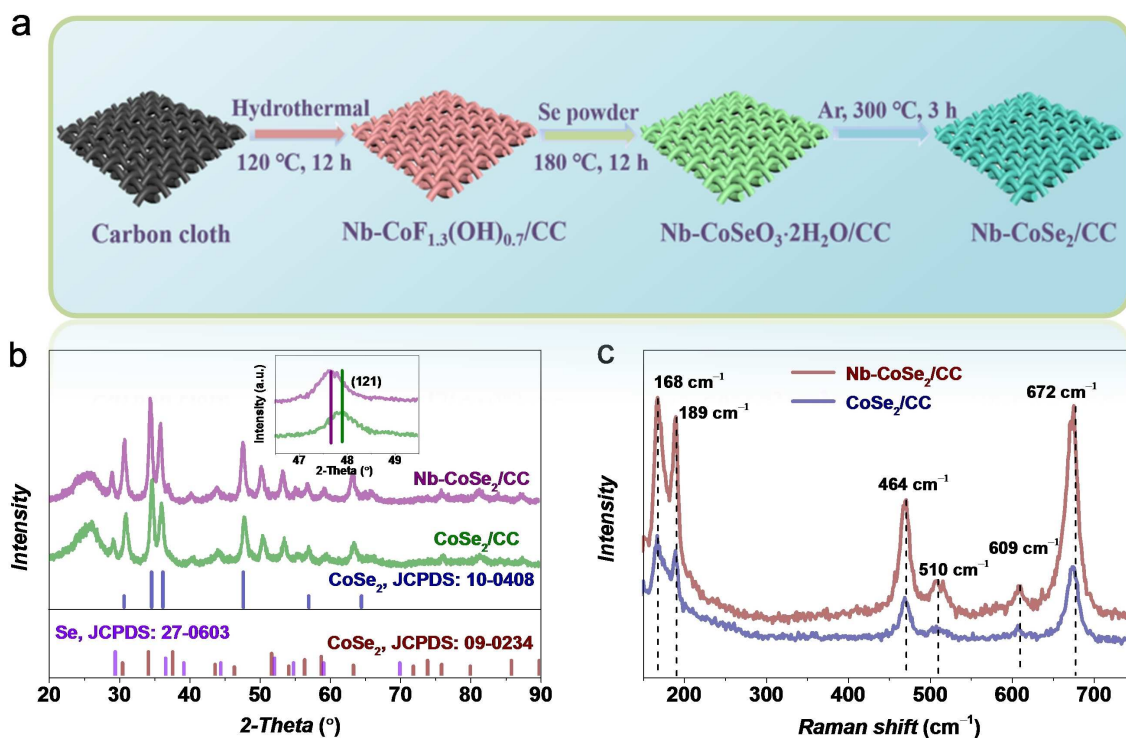


Figure 1. (a) Schematic illustration showing the formation of the Nb–CoSe₂/CC nanothorns. (b) XRD patterns of CoSe₂/CC and Nb–CoSe₂/CC [the inset is the enlarged view of the (121) peak]. (c) Raman spectra of CoSe₂ and Nb–CoSe₂ samples.

XRD peaks are attributed to Se (JCPDS: 27-0603). Significantly, there are no peaks for Nb compounds, indicating that no new crystalline phase was produced in the synthesis procedure. However, as shown in the inset of Figure 1b, the diffraction peak of (121) shifted slightly, indicating the possible Nb dopant in CoSe_2 crystal lattice, and the peak width was narrowed, which implies that the grain size of CoSe_2 has increased.^[15] Simultaneously, the Nb– CoSe_2/CC displays more sharp peaks and higher intensity than CoSe_2/CC , implying that Nb– CoSe_2/CC is endowed with better crystallinity and conductivity, which is beneficial to accelerate charge transfer, thereby improving OER activity.^[17] Furthermore, we also performed XRD characterization for catalysts with different molar ratios prepared at different temperatures. These results disclosed that the difference in molar ratios did not affect the crystal form and structure of the catalysts; nevertheless, the catalyst could not be converted to CoSe_2 below a specific temperature (Figure S3). As shown in Figure 1c, four Raman characteristic peaks at about 189, 464, 510, and 672 cm^{-1} of Nb– CoSe_2/CC can be ascribed to the cubic CoSe_2 .^[18] Note that the Se–Se stretching mode (168 and 189 cm^{-1}) are the same. Yet, the Raman peaks at 464, 510, and 672 cm^{-1} of Nb– CoSe_2/CC appear slight positive shifts compared with CoSe_2/CC ,^[19] further demonstrating that Nb-incorporated with the CoSe_2/CC and charge transfer between Nb and Co.

The morphologies of the materials were characterized by scanning electron microscopy (SEM). Figure S4a shows that the surface of the cleaned CC is smooth. As evidenced in Figure 2a, Nb– CoSe_2 presented a uniform nanothorn morphology similar to the precursor (Figure S4b,c). In addition, we also carried out SEM imaging on catalysts treated with different amounts of NbCl_5 at different annealing temperatures. The results revealed

a similar morphology (Figure S5). Although CoSe_2 and Nb– CoSe_2 show approximately the same morphology, the Nb– CoSe_2 catalyst has a large electrochemical specific surface area, better hydrophilicity, improved conductivity, and electron transferability CoSe_2 by incorporated Nb. Transmission electron microscopy (TEM) and high-angle annular dark-field scanning electron microscopy (HAADF-STEM) were utilized to visualize the morphology better. Observation via TEM (Figure 2b) revealed a nanothorn morphology consistent with the SEM image. A high-resolution (HR)TEM image (Figure 2c) presented a series of lattice fringes with lattice spacings of 0.239 and 0.290 nm, assigned to (211) and (110) crystal planes of cubic and orthorhombic CoSe_2 , respectively.^[20] Significantly, the selected area electron diffraction (SAED) pattern of nanothorns also confirmed the polycrystalline structure.^[21] The crystal planes of (110) and (111) are orthorhombic CoSe_2 , while (211) and (311) correspond to cubic CoSe_2 .

Significantly, the SAED patterns of the nanothorns also confirmed polycrystalline structure,^[21] regardless of Nb incorporation (Figure 2d and Figure S6), manifesting the minimum disturbance of Nb-incorporated to the host's crystal structure. Meantime, the energy-dispersive X-ray (EDX) spectrum, HAADF-STEM, and corresponding elemental mapping images revealed the existence of uniformly dispersed Co, Nb, and Se throughout the Nb– CoSe_2/CC (Figure 2e,f). The inductively coupled plasma atomic emission spectrometry (ICP-AES) test (Table S1) revealed that the sample comprises Co (37.56%) and Nb (4.23%). Thereby, all the above characterizations suggest the construction of Nb– CoSe_2/CC catalyst.

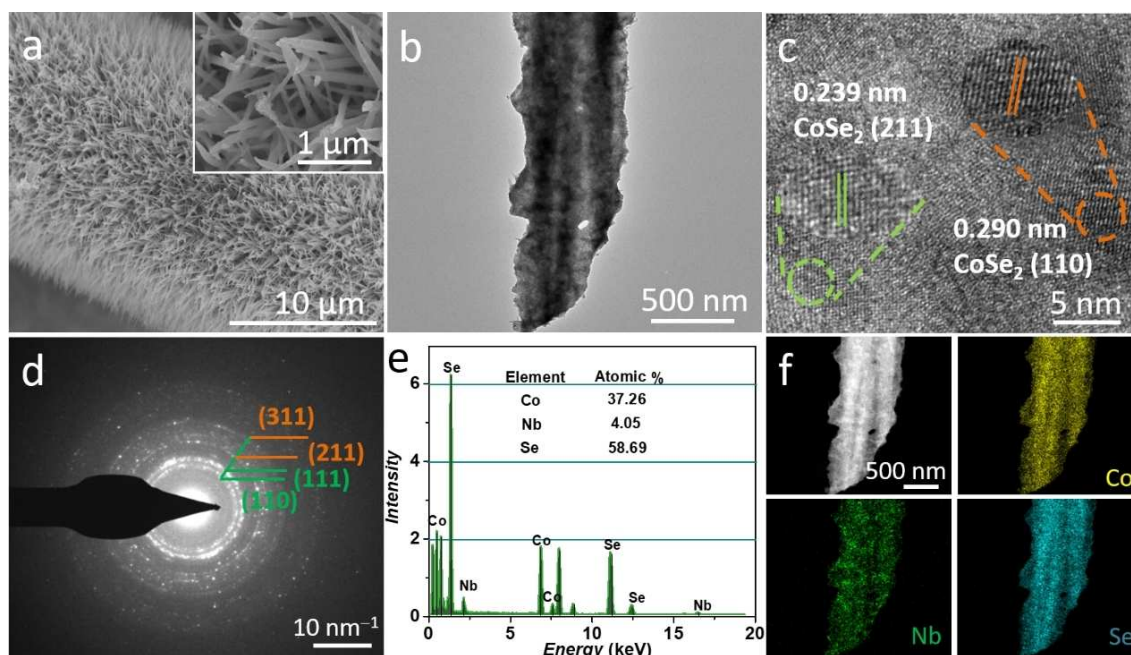


Figure 2. (a) SEM images and (b) TEM image of the Nb– CoSe_2/CC nanothorns. (c) HRTEM image. (d) SAED pattern. (e) EDX spectrum. (f) HAADF-STEM image and corresponding elemental mapping images of Nb– CoSe_2 nanothorns.

XPS analysis

The chemical composition and elemental valence states of CoSe_2/CC , $\text{Nb-CoSe}_2/\text{CC}$ before and after the OER stability test were explored by X-ray photoelectron spectroscopy (XPS). From Figure S7a, the characteristic peaks of C, O, Co, Nb, and Se elements in the $\text{Nb-CoSe}_2/\text{CC}$ manifest great consistency with XRD and TEM results. The C 1s spectra present three peaks at around 284.8, 286.0, and 286.5 eV, designated as C–, C–O, and C=O bonds (Figure S7b–d),^[22] respectively. The peaks located at 778.8–779.3 and 793.7–794.2 eV are ascribed to Co–Se bonds in $\text{Nb-CoSe}_2/\text{CC}$ and CoSe_2/CC (Figure 3a), demonstrating the successful synthesis of CoSe_2 . The two peaks located 781.4–781.7 and 797.2–797.5 eV correspond to the $\text{Co}^{2+} 2p_{3/2}$ and $\text{Co}^{2+} 2p_{1/2}$. The additional pairs at 785.3–785.7 and 802.6–803.1 eV accompanied by two satellite peaks indicate the near-optimal electronic configuration of antibonding orbital of Co–Se that relates to electroactivity.^[23] Meanwhile, the XPS peak attributed to the Co–Se bond in $\text{Nb-CoSe}_2/\text{CC}$ shows a slight negative shift of 0.5 eV compared to CoSe_2/CC , indicating an already established charge transfer from Co to Se in the $\text{Nb-CoSe}_2/\text{CC}$.^[24] Consequently, the positive charge increased of Co after Nb incorporated is beneficial to weaken and regulate the oxygen adsorption on the surface, thereby boosting the electrocatalytic activity.^[10] For the spectra of Se 3d, the peaks appearing at 54.5, 55.3, and 59.2 eV were assigned to $\text{Se} 3d_{5/2}$, $\text{Se} 3d_{3/2}$ of Co–Se, and Se-O_x bonds for CoSe_2 .^[25] The $\text{Se} 3d_{5/2}$ peaks of the Co–Se bonds for Nb-CoSe_2 exhibit a negative shift around 0.4 eV compared with CoSe_2 , meaning that positive charges of Se are reduced (Figure 3b). These results prove that Nb incorporation can well regulate the electron density of the

catalyst, which can significantly elevate the OER performance. In the Nb 3d XPS spectra, the peaks centered at 201.6 and 204.4 eV are allocated to $\text{Nb} 3d_{5/2}$ and $\text{Nb} 3d_{3/2}$ of metal Nb, and the binding energies of 207.1 and 209.9 eV correspond to Nb^{5+} .^[26] Notably, the binding energies of 198.0 and 199.6 eV are ascribed to $\text{Cl} 2p_{3/2}$ and $\text{Cl} 2p_{1/2}$, which are residual Cl element from NbCl_5 (Figure 3c).

Interestingly, the XPS peaks of the Co–Se and Se–Se bonds became much weaker after OER stability test. As we all know, transition metal selenide contains covalent bonds and ionic bonds, and the bond length of ionic bonds is much longer than that of covalent bonds. After OER stability test, the XPS peaks of Co–Se and Se–Se bonds became less obvious under strong oxidation conditions, confirming that the catalyst surface's covalent bond was transformed into an ionic bond, indicating that the active catalytic sites are ionic rather than covalent. After OER stability test, it can be observed that the peak of Nb^{5+} is more distinct, manifesting that the Nb atom at the surface was oxidized to high-valence Nb (hydro)oxide, which promotes the OER.^[14] Besides, we also performed Raman spectroscopy tests. It can be found that the composition of the catalyst surface undergoes a significant transformation after the OER stability test, mainly from CoSe_2 to Nb/Co (hydro)oxides/oxyhydroxides (Figure S8).^[27] This transition may be one of the important reasons for the degradation of the OER activity of the designed catalysts.

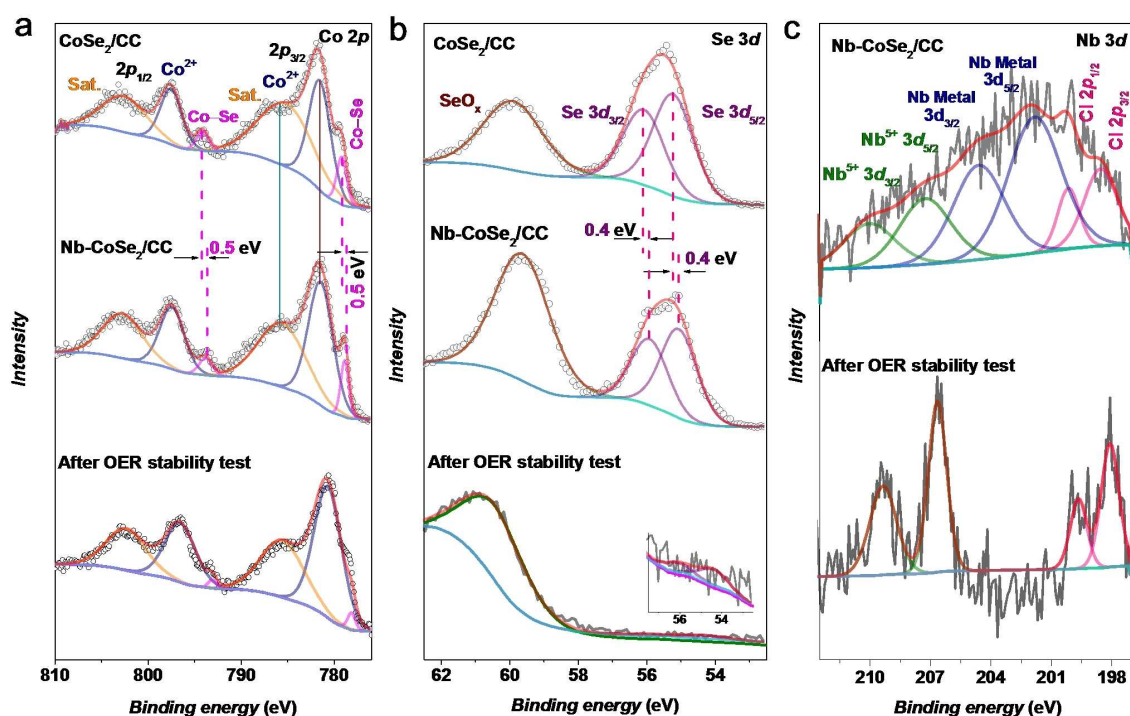


Figure 3. High-resolution XPS spectra of CoSe_2 , Nb-CoSe_2 , and after OER stability test. (a) Co 2p, (b) Se 3d, and (c) Nb 3d.

Electrochemical evaluation of Nb–CoSe₂/CC for OER

The OER catalytic activity of Nb–CoSe₂/CC was measured in a 1.0 M alkaline KOH solution at room temperature, along with four control samples. The self-supported catalysts can be directly used as a working electrode to examine the electrocatalytic performance without additional adhesive. Polarization curves (Figure 4a) illustrate that the Nb–CoSe₂/CC requires overpotential of 220 mV at 10 mA cm⁻², outperforming those of CoSe₂/CC (253 mV), Nb–CoSeO₃·2H₂O/CC (270 mV), Nb–CoF_{1.3}(OH)_{0.7}/CC (293 mV), and RuO₂/CC (243 mV). Moreover, the Nb–CoSe₂/CC delivered the ultra-low overpotential of 297 mV at a high current density of 200 mA cm⁻² and surpassed all the other electrocatalysts (Figure 4c).

The remarkable OER performance originated from the efficient synergy between Nb and CoSe₂ and the distinct nanothorn structure, providing sufficient porosity and larger surface area.^[28] Besides, the Tafel plots were calculated from linear sweep voltammetry (LSV) data to probe the OER reaction kinetics.^[29] The Tafel slopes of Nb–CoSe₂/CC, CoSe₂/CC, Nb–CoSeO₃·2H₂O/CC, Nb–CoF_{1.3}(OH)_{0.7}/CC, and RuO₂/CC are

54.1, 57.1, 58.1, 62.6, and 61.5 mV dec⁻¹, respectively (Figure 4b). The Nb–CoSe₂/CC manifests the smallest Tafel slope and favorable reaction dynamics. The excellent OER performance can be further clarified by the significantly smaller charge transfer resistance (R_{ct}) than others, as shown in Figure S9, revealing the fastest interfacial electron transfer and faster OER kinetics upon the Nb incorporation. The enhancement of charge transfer indicates that the nanothorn structure is essential for accelerating the electrolyte penetration and shortening the ion diffusion distance.^[21,30] As evidenced in Figure 4d and Table S2,^[7a,21,25,31] Nb–CoSe₂/CC is superior to various similar catalysts in the literature. In addition, we optimized annealing temperature and the Nb/Co molar ratio and found the optimal OER performance at 300 °C and Nb/Co ratio of 7:1 (Figures S10, S11).

To further understand the cause of the excellent OER catalytic activity of Nb–CoSe₂/CC, the double-layer capacitance (C_{dl}) values derived from cyclic voltammetry (CV) curves (Figures S12, S13) in the non-faradaic area were reported to evaluate the electrochemical surface area (ECSA). The C_{dl} is directly proportional to the ECSA, meaning the higher C_{dl} value,

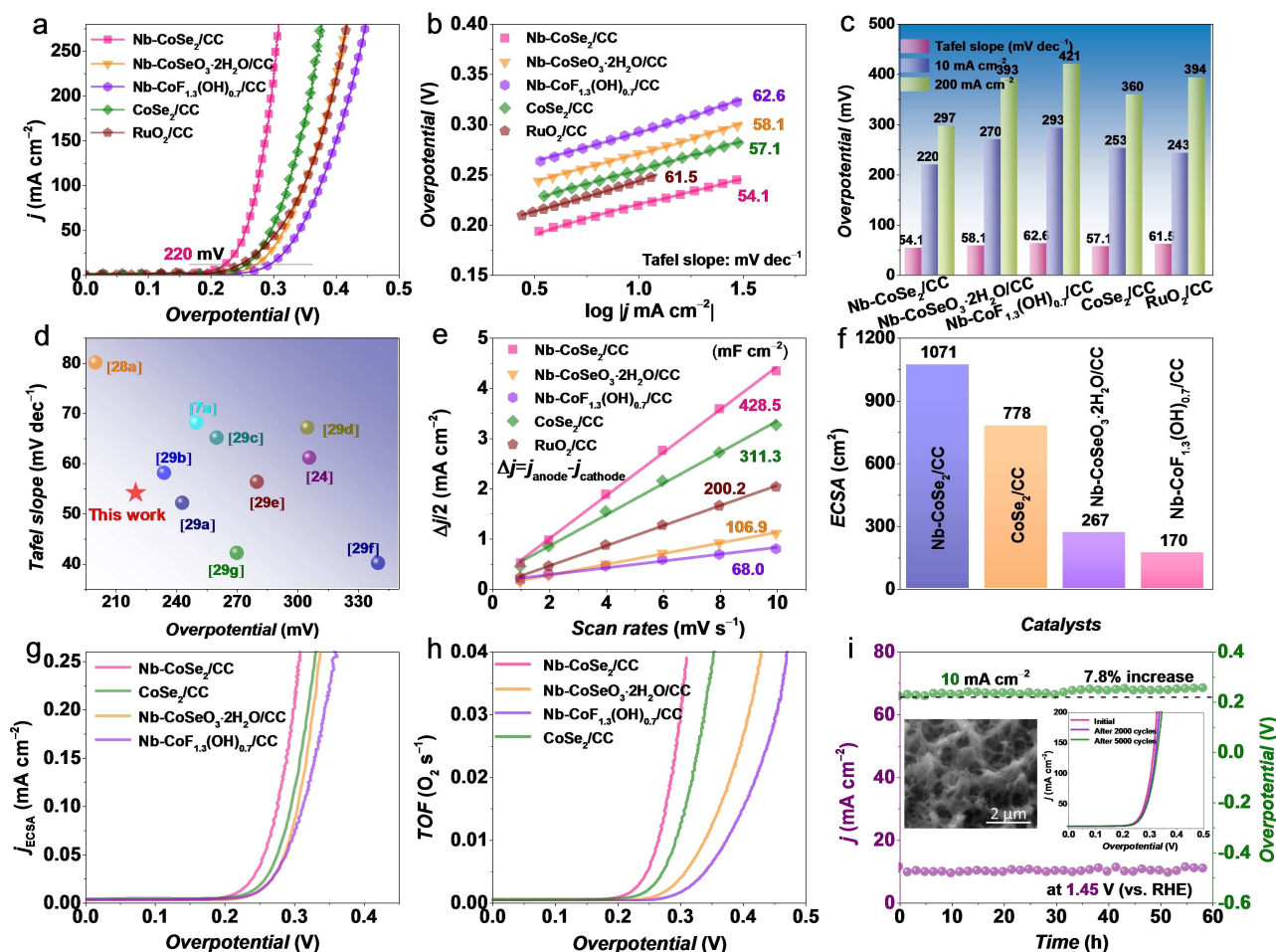


Figure 4. (a) LSV curves, (b) Tafel plots, (c) summary of overpotentials (at 10 and 200 mA cm⁻²) and Tafel plots. (d) Comparison of overpotential (at 10 mA cm⁻²) and Tafel plot for various state-of-the-art OER catalysts. (e) C_{dl} . (f) Comparison of ECSA for four catalysts. (g) ECSA-normalized LSV curves of the four catalysts. (h) Potential-dependent TOF curves. (i) Stability of the Nb–CoSe₂/CC nanothorns catalyst for OER (the inset shows the corresponding LSV curves of the Nb–CoSe₂/CC catalyst at different cycles; the image displays the morphology of the Nb–CoSe₂/CC nanothorns after OER).

the larger ECSA. The ECSA values can be calculated by the following Equation (1):

$$\text{ECSA} = \frac{C_{\text{dl}}}{C_s} \quad (1)$$

where C_s is the capacitance per unit area of a smooth surface of an electrocatalyst material.

As shown in Figure 4e, the C_{dl} of Nb–CoSe₂/CC is 428.5 mF cm⁻², which is much larger than those of CoSe₂/CC (311.3 mF cm⁻²), Nb–CoSeO₃·2H₂O/CC (106.9 mF cm⁻²), Nb–CoF_{1.3}(OH)_{0.7}/CC (68.0 mF cm⁻²), and RuO₂/CC (200.2 mF cm⁻²), respectively. The C_s are usually acquired in 20–60 μF cm⁻² to calculate the ECSA value in 1.0 M KOH solution. We used the average value of C_s (40 μF cm⁻²) in this work.^[32] The result revealed that the ECSA value of Nb–CoSe₂/CC is 1071 cm⁻² (Figure 4f and Table 1), which is 1.4-, 4.0-, and 6.3-fold larger than those of CoSe₂/CC, Nb–CoSeO₃·2H₂O/CC, and Nb–CoF_{1.3}(OH)_{0.7}/CC. The largest ECSA implies that introducing the Nb atom could effectively increase the number of active sites and maximize the chance of contact between active components and reactants, thereby accelerating the OER process.^[30] Furthermore, the geometric current density was further normalized by ECSA to compare the intrinsic activity. Intriguingly, the Nb–CoSe₂/CC displays the highest electrocatalytic performance and the highest intrinsic activity toward OER (Figure 4g). ICP results are used to estimate the turnover frequency (TOF) to evaluate further the intrinsic activity of electrocatalysts according to Equation (2).^[33]

$$\text{TOF} = \frac{j \times A}{4Fn} \quad (2)$$

where j is the current density, A is the electrode area with moles of catalyst, F is the Faraday constant (96485 C mol⁻¹), and n is the number of active sites of all metals present in the electrode. Strikingly, the TOF value of Nb–CoSe₂/CC increased more rapidly in contrast to CoSe₂/CC, Nb–CoSeO₃·2H₂O/CC, and Nb–CoF_{1.3}(OH)_{0.7}/CC when the applied potential increases. The TOF of Nb–CoSe₂/CC was calculated to be 0.01 s⁻¹ at an overpotential of 250 mV, which is much higher than other catalysts (Figure 4h). Thus, the highest TOF value further manifests the excellent OER intrinsic electrocatalyst activity.^[34] Overall, the outstanding OER activity of Nb–CoSe₂/CC could be reasonably explained by the high intrinsic catalytic property (lowest Tafel plot), the sufficient of active sites (largest ECSA), and the fast charge transferability (smallest R_{ct}).

Table 1. Summarized OER catalytic parameters of different catalysts in 1.0 M KOH electrolyte.

Catalyst	η_{10} [mV]	Tafel slope [mV dec ⁻¹]	C_{dl} [mF cm ⁻²]	R_{ct} [Ω]
Nb–CoSe ₂ /CC	220	54.1	428.5	0.7
CoSe ₂ /CC	253	57.1	311.3	1.0
Nb–CoSeO ₃ ·2H ₂ O/CC	270	58.1	106.9	1.2
Nb–CoF _{1.3} (OH) _{0.7} /CC	293	62.6	68.0	2.1
RuO ₂ /CC	243	61.5	200.2	1.3

Besides outstanding electrochemical activity, robust durability is an essential requirement in practical applications. Long-term stability of the OER optimized Nb–CoSe₂/CC was tested under a galvanostatic operation condition at 10 mA cm⁻² and chronoamperometry at a constant applied potential [1.45 V vs. reversible hydrogen electrode (RHE)] over 60 h. As depicted in Figure 4i, the current density decreased slightly in the first few hours and then gradually stabilized; concurrently, a potential increase of about 7.8% was detected at the stabilized current density after 60 h. Furthermore, an accelerated CV cycling test was conducted to investigate the catalytic robustness, and the sample revealed a negligible shift of polarization curves after cycling 2000 and 5000 CVs (inset of Figure 4i). Such remarkable stability of Nb–CoSe₂/CC can be attributed to the fact that Nb–CoSe₂/CC was anchored on conductive carbon cloth, inhibiting the aggregation of active sites, thereby improving the catalyst stability. Further insights into the morphology of Nb–CoSe₂/CC after OER stability test, confirming the nanothorn structure is well maintained and progressively evolved into a porous structure. Based on the above analysis, Nb–CoSe₂/CC is a potential candidate for highly efficient electrocatalytic water splitting.

Overall water splitting and contact angle test

Given the excellent OER electrocatalytic properties of the Nb–CoSe₂/CC catalyst, an electrolyzer was constructed for the overall water splitting experiment using Nb–CoSe₂/CC as anode and commercial Pt/C as the cathode (Figure 5a). Surprisingly, the Nb–CoSe₂/CC (+) | Pt/C (–) device only requires a low cell voltage of 1.52 V to achieve a current density of 10 mA cm⁻², which is same as commercial RuO₂ (+) | Pt/C (–) (1.51 V) (Figure 5b). However, the Nb–CoSe₂/CC (+) | Pt/C (–) catalyst surpasses the RuO₂ (+) | Pt/C (–) system at a high current density essential for industrial application. The inset of Figure 5b indicates the considerable stability for overall water splitting, maintaining 120 h with a negligible decrease in voltage. Moreover, the as-prepared electrolyzer was compared with the recently reported two-electrode catalytic device. The result showed that the cell voltage reached 10 mA cm⁻² current density, which was significantly lower than most two-electrode systems (Figure 5c and Table S3).^[16,35] In addition, we conducted tests under simulated industrial conditions and evaluated the catalyst performance in the 30 wt% KOH electrolyte. As demonstrated in Figure 5d, the Nb–CoSe₂/CC (+) | Pt/C (–) electrolyzer only demands 1.93 and 2.04 V cell voltage to drive high current densities of 500 and 1000 mA cm⁻², respectively. Strikingly, the electrolyzer shows impressive durability at 500 mA cm⁻² up to 24 h without an increase in cell voltage; these results indicate that the Nb–CoSe₂/CC composite is an ideal candidate to replace commercial noble metal electrocatalysts to achieve practical overall water splitting.^[36]

The nitrogen adsorption/desorption isotherm of Nb–CoSe₂/CC can be identified as a type III isotherm (Figure 6a,b and Figure S14), illustrating the presence of the hierarchical porous structure.^[37] Among them, mesopores are mainly originated

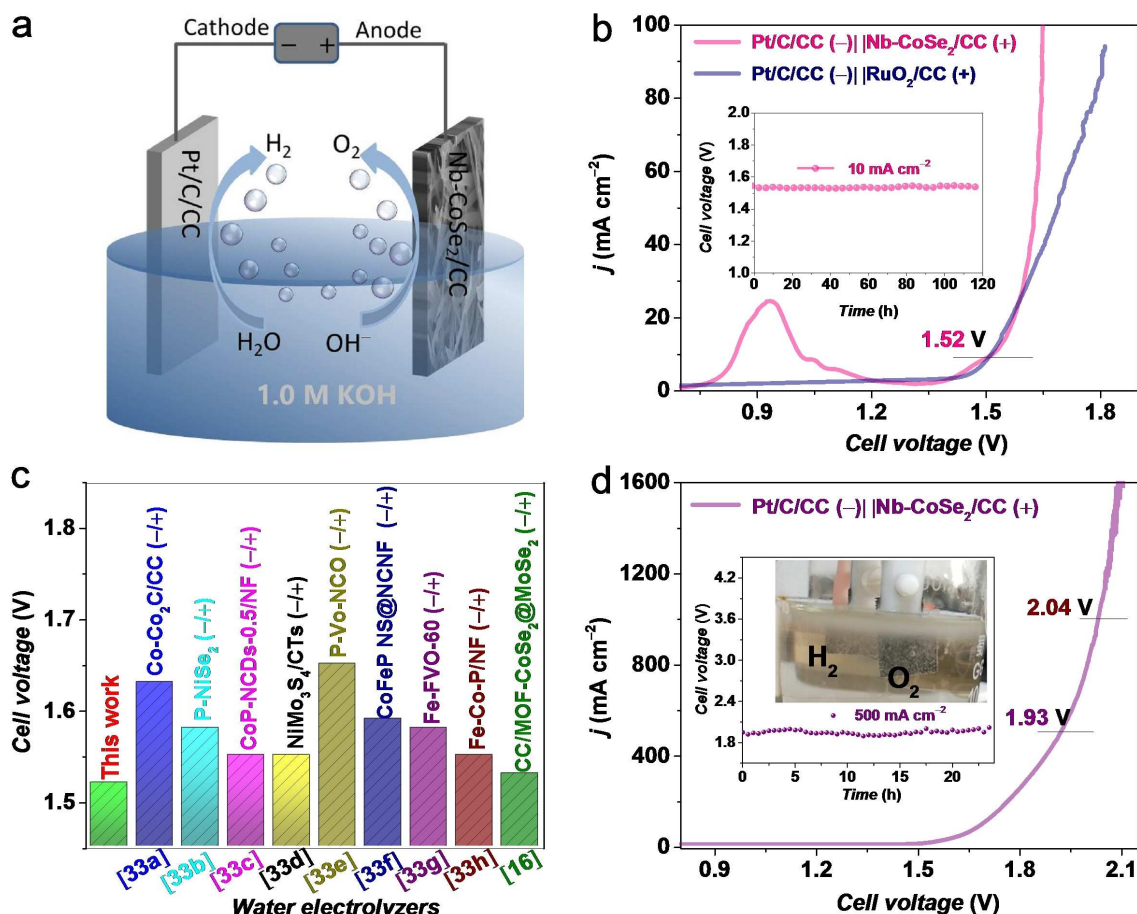


Figure 5. (a) Schematic diagram of overall water splitting in the two-electrode system. (b) Polarization curves of the two-electrode system in 1.0 M KOH (inset: current density vs. time curve of the two-electrode system). (c) Comparison of the voltages at 10 mA cm^{-2} with previously reported catalysts in 1.0 M KOH. (d) Polarization curve by two-electrode system of Nb–CoSe₂/CC (+) | Pt/C (–) in 30 wt% KOH electrolyte (inset: chronopotentiometry curve at a current density of 500 mA cm^{-2} and the digital photograph of the two-electrode system).

from the large number of voids left by the shrinkage and collapse of Nb–CoSe₂ nanothorns.^[38] The Brunauer-Emmett-Teller (BET) results demonstrate that Nb–CoSe₂/CC ($15.1 \text{ m}^2 \text{ g}^{-1}$) is endowed with the largest surface area compared with CoSe₂/CC ($4.9 \text{ m}^2 \text{ g}^{-1}$) and other counterparts, implying Nb–CoSe₂/CC is expected to expose more active sites. Furthermore, the Nb–CoSe₂/CC possesses a relatively broad pore distribution with an average pore size of about 28.9 nm (insert of Figure 6a,b and Figure S14), while the total pore volume is $0.108 \text{ cm}^3 \text{ g}^{-1}$. The above results reveal that Nb–CoSe₂/CC exhibits outstanding performance toward OER electrocatalysis due to the abundant active sites and diffusion channels for mass transfer.^[39]

DFT calculations

To further elucidate the OER reaction process mechanism of the catalyst, we performed DFT calculations based on the theoretical model. In this study, the models of pristine CoSe₂ and Nb–CoSe₂ were established and calculated to represent their

true phase states, respectively (Figure S15). According to the XRD results and the high stability of the CoSe₂ crystal plane, the (110) crystal plane of CoSe₂ was selected for DFT calculation.^[31b] First of all, the effect of Nb incorporated on electronic properties was investigated by calculating the electron density differences.^[40] The introduction of Nb atoms can profoundly adjust the electronic structure of CoSe₂ (Figure 7a). Since the highest electronegativity of the Nb atom among all elements becomes the electron depletion center, the effect of losing electrons in this reaction is more prominent. Compared with pure CoSe₂, due to the strong interaction between electrons, the charge near the Se atom increases, which is the center of charge accumulation, while the charge near the Co atom also decreases slightly.

Moreover, the density of states (DOS) of Nb-incorporated CoSe₂ and pristine CoSe₂ models are also calculated to provide insight into the internal Nb effect in the catalyst.^[41] As shown in Figure 7b,c, the d-band center position of Nb–CoSe₂ is moved up to -0.823 eV compared with the pristine CoSe₂ ($\epsilon_{\text{d}} = -0.985 \text{ eV}$), which indicates that the incorporation of Nb atom contributes to more optimal adsorption *OH and is therefore

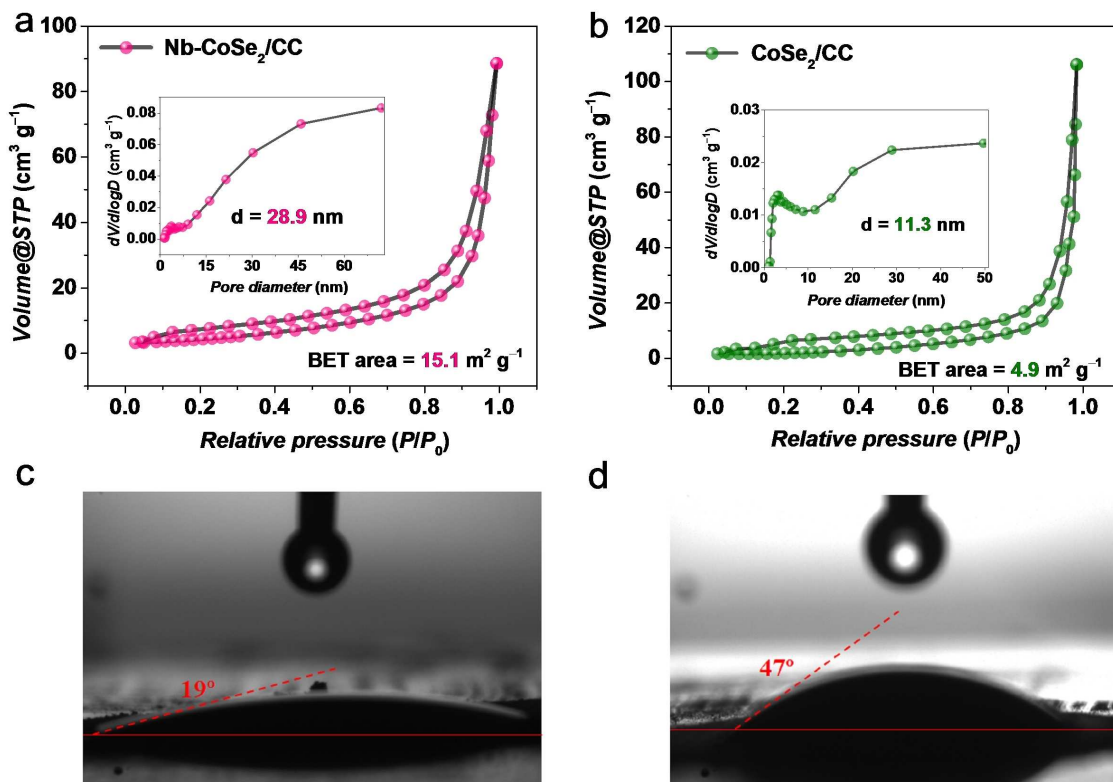


Figure 6. N₂ adsorption/desorption isotherms and pore size distributions (inset) for (a) Nb-CoSe₂/CC and (b) CoSe₂/CC. Contact angles of (c) Nb-CoSe₂/CC and (d) CoSe₂/CC.

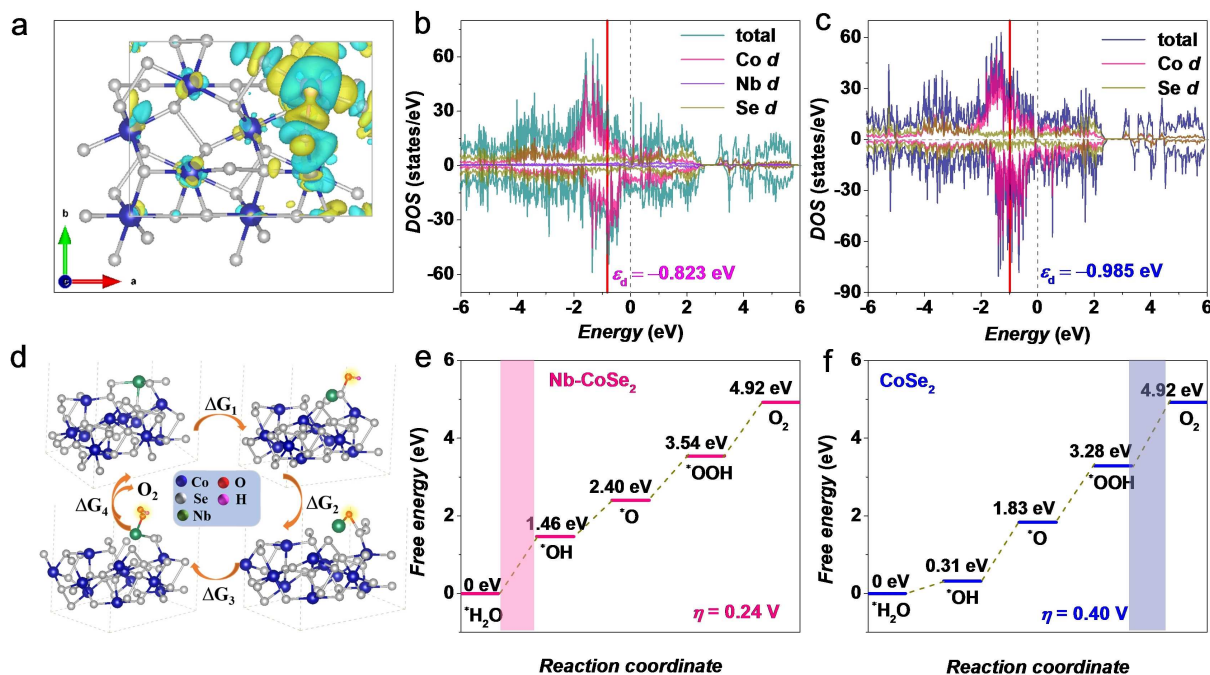


Figure 7. DFT calculations results. (a) Schematic diagram of differential charge structure model. The blue, green, and silver balls represent the Co, Nb, and Se atoms, respectively (yellow and green colors are electron accumulation and depletion). (b,c) DOS of Nb-CoSe₂ and CoSe₂. (d) Schematic profile of adsorption atomic configuration during the OER elementary steps. (e,f) Free energy diagrams of Nb-CoSe₂ and CoSe₂ for alkaline OER.

conductive to the following reaction. In addition, Nb-incorporated CoSe₂ makes the electron density of the orbital favorable for the orbital to be closer to the Fermi level, which improves the reactivity of Co atom and accelerates the OER process.^[42]

To better understand the effect of Nb atom doping on the OER process, we constructed different structural models of Nb–CoSe₂ in different states according to the OER reaction pathway. We calculated the reaction free energy diagram according to the four-electron transfer pathway (Figure 7d and Figure S16). The free energy of Nb–CoSe₂ and CoSe₂ calculated among the alkaline OER is shown in Figure 7e,f. The rate-determining step (RDS) to determine the OER on pristine CoSe₂ is the conversion of *OOH to O₂ with $\Delta G=1.64$ eV, which is equivalent to a theoretical overpotential of 0.40 V; this shows that pure CoSe₂ has lower catalytic activity for OER.^[43] Encouragingly, we found that under the coordination of Nb atom, the first energy barrier of Nb–CoSe₂ has 1.46 eV as the RDS, which is lower than the 1.64 eV of the pure CoSe₂ phase. The corresponding theoretical overpotential is 0.24 V. Hence, DFT calculations suggest that the Nb dopants can regulate the adsorption free energy of reaction intermediates and reduce the energy barrier for OER, playing an essential role in both tuning the CoSe₂ atomic structure and OER catalytic activity.^[9a]

The contact angles of Nb–CoSe₂ and CoSe₂ (Figure 6c,d) were measured to evaluate the surface wettability. The lower contact angle implies porous surface morphology and access defects that bind to the water molecule. The measurements illustrate that the contact wetting angle of Nb–CoSe₂ is 19°, while that of CoSe₂ is 47°, demonstrating that the Nb–CoSe₂ possesses better hydrophilicity. The increase in hydrophilicity may be due to the Nb incorporated, resulting in many defects on the catalyst surface.^[44] Furthermore, the super-hydrophilicity can promote deep wetting among the electrolyte and the catalyst, which helps the electrolyte enter the pores increase the possibility of contact between active sites and reactants.^[45]

As discussed above, the reasons for the unusual OER activity of Nb–CoSe₂/CC are ascribed to the following points. (1) The DFT calculations suggest that Nb incorporating modification promoted the conductivity and electron transfer ability of CoSe₂ nanothorns, in addition to tune the d-band center and endow CoSe₂ nanothorns with abundant reaction sites.^[46] (2) Nb incorporating also adjusts the *OH adsorption energy and lowers the energy barrier from M to M–OH for the catalyst, which significantly promotes the OER process.^[47] (3) The Nb–CoSe₂ possesses a nanothorn structure with a high specific surface area, maximizing the exposure of active sites and providing effective electronic and ionic transport paths, thus improving the OER activity.^[31g] (4) The super-hydrophilic nature of the Nb–CoSe₂ catalyst can boost the electrolyte affinity and permeation, and increase the probability of interaction between the active sites and the reactants.^[48]

Conclusions

We reported a rational design and synthesis of the self-supported Nb–CoSe₂/CC (CC=carbon cloth) electrocatalyst

with a nanothorn structure. We discovered the positive effect of the Nb atom as a catalytic promoter on the OER performance. Benefiting from the distinct structure and compositional superiorities, the Nb–CoSe₂/CC achieved low overpotentials of 220 and 297 mV at the current density of 10 and 200 mA cm^{−2}, respectively. The small Tafel slope of 54.1 mVdec^{−1} demonstrates fast reaction kinetics. Besides, Nb–CoSe₂/CC (+) || Pt/C (−) electrolyzer required only 1.52 V to accomplish the current density of 10 mA cm^{−2}, displaying excellent long-term stability for overall water splitting at both low and high current density. Characteristic studies proved that the strong interaction between Nb atom and CoSe₂ enabled more active sites and reaction centers. As demonstrated by density functional theory calculations, the Nb atom can well optimize the d-band center and electronic state of Nb–CoSe₂, which is beneficial to charge transfer, adsorption of oxygen-containing intermediates, and O₂ desorption in the OER process. In short, this work provides a valuable platform for the rational design of OER electrocatalysts application by incorporated with other unconventional elements.

Experimental Section

Chemicals and materials

Cobalt nitrate hexahydrate [Co(NO₃)₂·6H₂O, 99.0%, Aladdin, 500 g], niobium chloride (NbCl₅, 99.0%, Macklin, 5 g), ammonium fluoride (NH₄F, 98.0%, Aladdin, 250 g), urea (CH₄N₂O, 99.0%, Xilong, 500 g), selenium powder (Se, 99.99%, Aladdin, 25 g), sodium borohydride (NaBH₄, 98.0%, Xilong, 100 g), potassium hydroxide (KOH, 90.0%, Macklin, 500 g), hydrochloric acid (HCl, 37.0%, Xilong, 500 mL), ethanol (C₂H₅OH, 99.7%, Xilong, 500 mL). All the chemicals were used directly without further purification. Carbon cloth (CC, W051009, 0.33×400×400 mm) was purchased from a commercial company. The Nafion solution (5 wt%) and commercial Pt/C (20 wt% Pt, Sinero, 1 g) were purchased from Alfa Aesar. The RuO₂ powder was prepared by directly annealing RuCl₃·3H₂O (37.0%, Inno-chem, 25 g). The water used in all experiments was prepared by passing through an ultra-pure purification system.

Synthesis of Nb–CoF_{1.3}(OH)_{0.7}/CC

In a typical procedure, the CC (2 cm×3 cm) was cleaned in dilute HCl solution, deionized water, and ethanol by ultrasonic treatment before the reaction to ensure that the surface was clean. Briefly, 1.75 mmol Co(NO₃)₂·6H₂O, 0.25 mmol NbCl₅, 10 mmol CH₄N₂O, and 4 mmol NH₄F were dissolved in 30 mL deionized water and stirred for 30 min to form a clear solution. The above solution and CC were transformed into a 50 mL Teflon-lined stainless-steel autoclave and heated in an electric oven at 120 °C for 12 h. After the autoclave was naturally cooled down to room temperature, the Nb–CoF_{1.3}(OH)_{0.7}/CC was washed with deionized water and ethanol to remove surface impurities and then dried in an oven at 60 °C for 6 h.

Synthesis of Nb–CoSeO₃·2H₂O/CC

Initially, 2 mmol Se powder and 4 mmol NaBH₄ were added into 30 mL deionized water and continued stirring for 30 min to form a homogeneous solution under magnetic stirring. Then it was poured

into a 50 mL Teflon-lined stainless-steel autoclave with the resulting Nb–CoF_{1.3}(OH)_{0.7}/CC. The autoclave was sealed and maintained at 180 °C for 12 h. After cooling to room temperature, the Nb–CoSeO₃·2H₂O/CC was washed with deionized water and ethanol several times and then dried at 60 °C for 6 h.

Synthesis of Nb–CoSe₂/CC

The as-prepared Nb–CoSeO₃·2H₂O/CC was placed into a porcelain boat and annealed at 300 °C for 3 h with a heating rate of 5 °C min⁻¹ under the pure Ar atmosphere. After naturally cooling room temperature, the obtained product was named Nb–CoSe₂/CC. The average loading of Nb–CoSe₂/CC was about 3.3 mg cm⁻². In addition, we controlled the total amount of metal to be 2 mmol and carried out a series of ratio adjustments. The CoSe₂/CC, Nb_{0.125}-CoSe₂/CC, and Nb_{0.5}-CoSe₂/CC were obtained by varying the molar ratios of Co/Nb in the hydrothermal solution to 2:0, 15:1, and 3:1, respectively.

Electrochemical measurements

All electrochemical measurements were performed on a Biologic VMP3 electrochemical workstation equipped with a standard three-electrode system in 1.0 M KOH (pH ≈ 13.8) electrolyte. The electrode (1 cm × 1 cm), graphite plate, and saturated calomel electrode (SCE) were employed as the working, counter, and reference electrodes. CV tests to stabilize the catalyst performance were performed at a scan rate of 10 mV s⁻¹. C_{dl} of the electrocatalysts were measured by CV at different scan rates, and calculated according to Equation (3):

$$C_{dl} = \frac{j_a - j_c}{2 \times \nu} \quad (3)$$

where j_a and j_c correspond to the current density of anode and cathode, respectively, and ν is the scan rate. The C_{dl} was used to measure the ECSA. LSV was conducted for OER polarization curves with a sweeping rate of 0.5 mV s⁻¹. Electrochemical impedance spectroscopy (EIS) measurements were collected with a frequency range from 0.01 Hz to 200 kHz. All potentials (vs. SCE) were calibrated and converted to RHE by the Nernst equation [Eq. (4)] (Figure S1):

$$E_{RHE} = E_{SCE} + 0.242 + 0.059 \times \text{pH} \quad (4)$$

The overall water splitting test was implemented in a two-electrode system in a voltage range of 0–2.0 V (vs. SCE) with a scan rate of 5 mV s⁻¹ in 1.0 M KOH and 30 wt% KOH electrolyte, and all reported curves were corrected against *iR* compensation.

Acknowledgements

This work has been supported by the National Natural Science Foundation of China (no. 21965005), the Natural Science Foundation of Guangxi Province (2018GXNSFAA294077, 2021GXNSFAA076001), the Project of High-Level Talents of Guangxi (F-KA18015), and Guangxi Technology Base and Talent Subject (GUIKE AD18126001, GUIKE AD20297039).

Conflict of Interest

The authors declare no conflict of interest.

Data Availability Statement

Research data are not shared.

Keywords: electrochemistry · electron transfer · oxygen evolution reaction · super-hydrophilicity · water electrolysis

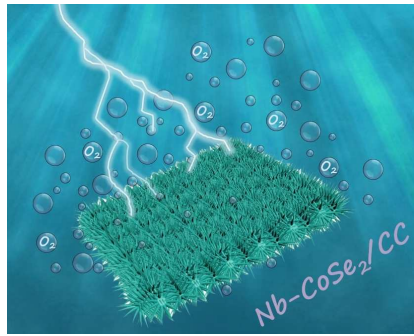
- [1] a) W. Cheng, S. Xi, Z.-P. Wu, D. Luan, X. W. D. Lou, *Sci. Adv.* **2021**, *7*, eabk0919; b) J. Yang, Y. Wang, J. Yang, Y. Pang, X. Zhu, Y. Lu, Y. Wu, J. Wang, H. Chen, Z. Kou, Z. Shen, Z. Pan, J. Wang, *Small* **2021**, *36*, 2106187; c) X. Gao, L. Yin, L. Zhang, Y. Zhao, B. Zhang, *Chem. Eng. J.* **2020**, *395*, 125058.
- [2] a) J. Nai, X. Xu, Q. Xie, G. Lu, Y. Wang, D. Luan, X. Tao, X. W. D. Lou, *Adv. Mater.* **2021**, *1*, 2104405; b) J. Hu, A. Al-Salihy, J. Wang, X. Li, Y. Fu, Z. Li, X. Han, B. Song, P. Xu, *Adv. Sci.* **2021**, *8*, 2103314.
- [3] a) H. Yang, Z. Chen, W. Hao, H. Xu, Y. Guo, R. Wu, *Appl. Catal. B* **2019**, *252*, 214–221; b) K. Shah, R. Dai, M. Mateen, Z. Hassan, Z. Zhuang, C. Liu, M. Israr, W. C. Cheong, B. Hu, R. Tu, C. Zhang, X. Chen, Q. Peng, C. Chen, Y. Li, *Angew. Chem. Int. Ed.* **2021**, *52*, 202114951.
- [4] a) R. Qin, P. Wang, Z. Li, J. Zhu, F. Cao, H. Xu, Q. Ma, J. Zhang, J. Yu, S. Mu, *Small* **2021**, *25*, 2105305; b) H. Zhong, G. Gao, X. Wang, H. Wu, S. Shen, W. Zuo, G. Cai, G. Wei, Y. Shi, D. Fu, C. Jiang, L. W. Wang, F. Ren, *Small* **2021**, *17*, 2103501; c) L. Zhang, Y. Lei, D. Zhou, C. Xiong, Z. Jiang, X. Li, H. Shang, Y. Zhao, W. Chen, B. Zhang, *Nano Res.* **2022**, *15*, 2895–2904.
- [5] a) L. Huang, D. Chen, G. Luo, Y. R. Lu, C. Chen, Y. Zou, C. L. Dong, Y. Li, S. Wang, *Adv. Mater.* **2019**, *31*, 1901439; b) C. Panda, P. W. Menezes, M. Zheng, S. Orthmann, M. Driess, *ACS Energy Lett.* **2019**, *4*, 747–754; c) Q. Wang, X. Huang, Z. L. Zhao, M. Wang, B. Xiang, J. Li, Z. Feng, H. Xu, M. Gu, *J. Am. Chem. Soc.* **2020**, *142*, 7425–7433; d) K. Wan, J. Luo, C. Zhou, T. Zhang, J. Arbiol, X. Lu, B. W. Mao, X. Zhang, J. Franssaer, *Adv. Funct. Mater.* **2019**, *29*, 1900315; e) Y. Tong, H. Guo, D. Liu, X. Yan, P. Su, J. Liang, S. Zhou, J. Liu, G. Q. M. Lu, S. X. Dou, *Angew. Chem. Int. Ed.* **2020**, *59*, 7356–7361; *Angew. Chem.* **2020**, *132*, 7426–7431.
- [6] Y. Zhao, H. Cong, P. Li, D. Wu, S. Chen, W. Luo, *Angew. Chem. Int. Ed.* **2021**, *60*, 7013–7017.
- [7] a) D. Xu, X. Long, J. Xiao, Z. Zhang, G. Liu, H. Tong, Z. Liu, N. Li, D. Qian, J. Li, J. Liu, *Chem. Eng. J.* **2021**, *422*, 129982; b) Q. Li, Z. Xing, A. M. Asiri, P. Jiang, X. Sun, *Int. J. Hydrogen Energy* **2014**, *39*, 16806–16811.
- [8] K. Li, J. Zhang, R. Wu, Y. Yu, B. Zhang, *Adv. Sci.* **2016**, *3*, 1500426.
- [9] a) Z. Chen, R. Zheng, M. Graš, W. Wei, G. Lota, H. Chen, B.-J. Ni, *Appl. Catal. B* **2021**, *288*, 120037; b) Y. Huang, L. W. Jiang, B. Y. Shi, K. M. Ryan, J. J. Wang, *Adv. Sci.* **2021**, *21*, 2101775; c) Y. Liu, J. Zhang, Y. Li, Q. Qian, Z. Li, Y. Zhu, G. Zhang, *Nat. Commun.* **2020**, *11*, 1853.
- [10] W. Li, Y. Jiang, Y. Li, Q. Gao, W. Shen, Y. Jiang, R. He, M. Li, *Chem. Eng. J.* **2021**, *425*, 130651.
- [11] S. Wen, G. Chen, W. Chen, M. Li, B. Ouyang, X. Wang, D. Chen, T. Gong, X. Zhang, J. Huang, K. Ostrikov, *J. Mater. Chem. A* **2021**, *9*, 9918–9926.
- [12] Y.-N. Zhou, F.-L. Wang, S.-Y. Dou, Z.-N. Shi, B. Dong, W.-L. Yu, H.-Y. Zhao, F.-G. Wang, J.-F. Yu, Y.-M. Chai, *Chem. Eng. J.* **2022**, *427*, 131643.
- [13] L. Zhang, J. Zhang, J. Fang, X. Y. Wang, L. Yin, W. Zhu, Z. Zhuang, *Small* **2021**, *17*, 2100832.
- [14] X. H. Chen, X. L. Li, L. L. Wu, H. C. Fu, J. Luo, L. Shen, Q. Zhang, J. L. Lei, H. Q. Luo, N. B. Li, *J. Mater. Chem. A* **2021**, *9*, 11563–11570.
- [15] X. H. Chen, Q. Zhang, L. L. Wu, L. Shen, H. C. Fu, J. Luo, X. L. Li, J. L. Lei, H. Q. Luo, N. B. Li, *Mater. Today Phys.* **2020**, *15*, 100268.
- [16] S. J. Patil, N. R. Chodankar, S.-K. Hwang, P. A. Shinde, G. Seeta Rama Raju, K. Shanmugam Ranjith, Y. S. Huh, Y.-K. Han, *Chem. Eng. J.* **2022**, *429*, 132379.
- [17] D. Chen, R. Lu, Z. Pu, J. Zhu, H.-W. Li, F. Liu, S. Hu, X. Luo, J. Wu, Y. Zhao, S. Mu, *Appl. Catal. B* **2020**, *279*, 119396.
- [18] X. Zhao, H. Zhang, Y. Yan, J. Cao, X. Li, S. Zhou, Z. Peng, J. Zeng, *Angew. Chem. Int. Ed.* **2017**, *56*, 328–332; *Angew. Chem.* **2017**, *129*, 334–338.
- [19] S. Zhang, J. Zhang, P. Liang, C. Zhang, T. Kou, Z. Zhang, *J. Power Sources* **2021**, *497*, 229895.

- [20] L. Yao, S. Ju, T. Xu, X. Yu, *ACS Nano* **2021**, *15*, 13662–13673.
- [21] X. Li, Z. Kou, S. Xi, W. Zang, T. Yang, L. Zhang, J. Wang, *Nano Energy* **2020**, *78*, 105230.
- [22] Q. Peng, Q. He, Y. Hu, T. T. Isimjan, R. Hou, X. Yang, *J. Energy Chem.* **2022**, *65*, 574–582.
- [23] M. Wang, L. Fan, X. Sun, B. Guan, B. Jiang, X. Wu, D. Tian, K. Sun, Y. Qiu, X. Yin, Y. Zhang, N. Zhang, *ACS Energy Lett.* **2020**, *5*, 3041–3050.
- [24] a) H. Wang, Y. Wang, J. Zhang, X. Liu, S. Tao, *Nano Energy* **2021**, *84*, 105943; b) Y. Cheng, J. Gong, B. Cao, X. Xu, P. Jing, B. Liu, R. Gao, J. Zhang, *ACS Catal.* **2021**, *11*, 3958–3974.
- [25] J. Yu, W.-J. Li, G. Kao, C.-Y. Xu, R. Chen, Q. Liu, J. Liu, H. Zhang, J. Wang, *J. Energy Chem.* **2021**, *60*, 111–120.
- [26] D. C. Nguyen, T. L. Luyen Doan, S. Prabhakaran, D. T. Tran, D. H. Kim, J. H. Lee, N. H. Kim, *Nano Energy* **2021**, *82*, 105750.
- [27] a) P. Gao, Y. Zeng, P. Tang, Z. Wang, J. Yang, A. Hu, J. Liu, *Adv. Funct. Mater.* **2021**, *32*, 2108644; b) L. She, F. Zhang, C. Jia, L. Kang, Q. Li, X. He, J. Sun, Z. Lei, Z. H. Liu, *J. Colloid Interface Sci.* **2020**, *573*, 1–10.
- [28] H. Liu, X. Ma, Y. Rao, Y. Liu, J. Liu, L. Wang, M. Wu, *ACS Appl. Mater. Interfaces* **2018**, *10*, 10890–10897.
- [29] M. Li, X. Pan, M. Jiang, Y. Zhang, Y. Tang, G. Fu, *Chem. Eng. J.* **2020**, *395*, 125160.
- [30] J. Nai, X. W. D. Lou, *Adv. Mater.* **2019**, *31*, 1706825.
- [31] a) M.-I. Jamesh, M. Harb, *J. Energy Chem.* **2021**, *56*, 299–342; b) J. Huang, S. Wang, J. Nie, C. Huang, X. Zhang, B. Wang, J. Tang, C. Du, Z. Liu, J. Chen, *Chem. Eng. J.* **2021**, *417*, 128055; c) Y.-J. Tang, Y. Wang, K. Zhou, *J. Mater. Chem. A* **2020**, *8*, 7925–7934; d) J. Wang, X. Zheng, Y. Cao, L. Li, C. Zhong, Y. Deng, X. Han, W. Hu, *ACS Appl. Mater. Interfaces* **2020**, *12*, 8115–8123; e) M. Ramadoss, Y. Chen, Y. Hu, B. Wang, R. Jayagopal, K. Marimuthu, X. Wang, D. Yang, *J. Mater. Sci. Technol.* **2021**, *78*, 229–237; f) C. Wang, R. Wang, Y. Peng, J. Chen, Z. Chen, H. Yin, J. Li, *J. Mater. Chem. A* **2020**, *8*, 24598–24607; g) Y. Zhang, C. Zhang, Y. Guo, D. Liu, Y. Yu, B. Zhang, *J. Mater. Chem. A* **2019**, *7*, 2536–2540.
- [32] C. C. McCrory, S. Jung, J. C. Peters, T. F. Jaramillo, *J. Am. Chem. Soc.* **2013**, *135*, 16977–16987.
- [33] Y. Pan, K. Sun, Y. Lin, X. Cao, Y. Cheng, S. Liu, L. Zeng, W.-C. Cheong, D. Zhao, K. Wu, Z. Liu, Y. Liu, D. Wang, Q. Peng, C. Chen, Y. Li, *Nano Energy* **2019**, *56*, 411–419.
- [34] a) B. Liu, Y. Wang, H. Q. Peng, R. Yang, Z. Jiang, X. Zhou, C. S. Lee, H. Zhao, W. Zhang, *Adv. Mater.* **2018**, *30*, 1803144; b) Q. Peng, X. Shao, C. Hu, Z. Luo, T. Taylor Isimjan, Z. Dou, R. Hou, X. Yang, *J. Colloid Interface Sci.* **2022**, *615*, 577–586.
- [35] a) P. Wang, J. Zhu, Z. Pu, R. Qin, C. Zhang, D. Chen, Q. Liu, D. Wu, W. Li, S. Liu, J. Xiao, S. Mu, *Appl. Catal. B* **2021**, *296*, 120334; b) W. Yang, S. Wang, K. Zhao, Y. Hua, J. Qiao, W. Luo, L. Li, J. Hao, W. Shi, *J. Colloid Interface Sci.* **2021**, *602*, 115–122; c) H. Liu, Z. Liu, Y. Wang, J. Zhang, Z. Yang, H. Hu, Q. Zhao, H. Ning, L. Zhi, M. Wu, *Carbon* **2021**, *182*, 327–334; d) D. Kong, Y. Wang, S. Huang, Y. V. Lim, M. Wang, T. Xu, J. Zang, X. Li, H. Y. Yang, *J. Colloid Interface Sci.* **2021**, *607*, 1876–1887; e) L. Zhang, J. Peng, W. Zhang, Y. Yuan, K. Peng, *J. Power Sources* **2021**, *490*, 229541; f) B. Wei, G. Xu, J. Hei, L. Zhang, T. Huang, Q. Wang, *J. Colloid Interface Sci.* **2021**, *602*, 619–626; g) F. Nur Indah Sari, S. Abdillah, J.-M. Ting, *Chem. Eng. J.* **2021**, *416*, 129165; h) H. Xu, J. Zhu, P. Wang, D. Chen, C. Zhang, M. Xiao, Q. Ma, H. Bai, R. Qin, J. Ma, S. Mu, *J. Mater. Chem. A* **2021**, *9*, 24677.
- [36] Y. Liu, X. Luo, C. Zhou, S. Du, D. Zhen, B. Chen, J. Li, Q. Wu, Y. Iru, D. Chen, *Appl. Catal. B* **2020**, *260*, 118197.
- [37] H. Liu, J. Guan, S. Yang, Y. Yu, R. Shao, Z. Zhang, M. Dou, F. Wang, Q. Xu, *Adv. Mater.* **2020**, *32*, 2003649.
- [38] K. Dai, N. Zhang, L. Zhang, L. Yin, Y. Zhao, B. Zhang, *Chem. Eng. J.* **2021**, *414*, 128804.
- [39] M. Liu, Q. He, S. Huang, W. Zou, J. Cong, X. Xiao, P. Li, J. Cai, L. Hou, *ACS Appl. Mater. Interfaces* **2021**, *13*, 9932–9941.
- [40] W. Cheng, X. F. Lu, D. Luan, X. W. D. Lou, *Angew. Chem. Int. Ed.* **2020**, *59*, 18234–18239; *Angew. Chem.* **2020**, *132*, 18391–18396.
- [41] Y. Yang, Q. Dai, L. Shi, Y. Liu, T. T. Isimjan, X. Yang, *J. Phys. Chem. Lett.* **2022**, *13*, 2107–2116.
- [42] K. Guo, Y. Wang, S. Yang, J. Huang, Z. Zou, H. Pan, P. S. Shinde, S. Pan, J. Huang, C. Xu, *Sci. Bull.* **2021**, *66*, 52–61.
- [43] Y. Hu, Z. Luo, M. Guo, J. Dong, P. Yan, C. Hu, T. T. Isimjan, X. Yang, *Chem. Eng. J.* **2022**, *435*, 134795.
- [44] a) D. Kim, X. Qin, B. Yan, Y. Piao, *Chem. Eng. J.* **2021**, *408*, 127331; b) P. Hou, D. Li, N. Yang, J. Wan, C. Zhang, X. Zhang, H. Jiang, Q. Zhang, L. Gu, D. Wang, *Angew. Chem. Int. Ed.* **2021**, *60*, 6926–6931.
- [45] Y. Sun, Y. Li, S. You, X. Li, Y. Zhang, Z. Cai, M. Liu, N. Ren, J. Zou, *Chem. Eng. J.* **2021**, *424*, 130460.
- [46] Y. Han, X. Chen, C. Qian, X. Zhang, W. He, H. Ren, H. Li, G. Diao, M. Chen, *Chem. Eng. J.* **2021**, *420*, 130461.
- [47] X. L. Zhang, P. P. Yang, Y. R. Zheng, Y. Duan, S. J. Hu, T. Ma, F. Y. Gao, Z. Z. Niu, Z. Z. Wu, S. Qin, L. P. Chi, X. Yu, R. Wu, C. Gu, C. M. Wang, X. S. Zheng, X. Zheng, J. F. Zhu, M. R. Gao, *Angew. Chem. Int. Ed.* **2021**, *60*, 6553–6560; *Angew. Chem.* **2021**, *133*, 6627–6634.
- [48] F. Cheng, L. Wang, H. Wang, C. Lei, B. Yang, Z. Li, Q. Zhang, L. Lei, S. Wang, Y. Hou, *Nano Energy* **2020**, *71*, 104621.

Manuscript received: April 26, 2022
Revised manuscript received: June 7, 2022
Accepted manuscript online: June 15, 2022
Version of record online: ■■■, ■■■■

RESEARCH ARTICLE

A thorny challenge: A nanothorn-like superhydrophilic Nb–CoSe₂/CC (CC = carbon cloth) catalyst is fabricated through a facile in-situ hydrothermal selenization and Ar annealing strategies. The catalyst illustrates an excellent oxygen evolution activity (297 mV at 200 mA cm⁻²), outstanding long-term durability, and good overall water splitting performance (1.93 V at 500 mA cm⁻²).



Q. Peng, X. Zhuang, L. Wei, L. Shi,
Dr. T. T. Isimjan*, Prof. R. Hou,
Prof. Dr. X. Yang*

1 – 12

Niobium-Incorporated CoSe₂ Nanothorns with Electronic Structural Alterations for Efficient Alkaline Oxygen Evolution Reaction at High Current Density

